Structure and transportation of electron vortices in near-critical density plasmas driven by ultrashort intense laser pulses

D N Yue[1,2], M Chen[1,2,*], P F Geng[1,2], X H Yuan[1,2], Z M Sheng[1,2,3,4], J Zhang[1,2], Q L Dong[5], A Das[6] and G R Kumar[7]

[1]Key Laboratory for Laser Plasmas (Ministry of Education), School of Physics and Astronomy, Shanghai Jiao Tong University, Shanghai 200240, China
[2]Collaborative Innovation Center of IFSA, Shanghai Jiao Tong University, Shanghai 200240, China
[3]SUPA, Department of Physics, University of Strathclyde, Glasgow G4 0NG, United Kingdom
[4]Tsung-Dao Lee Institute, Shanghai 200240, China
[5]School of Science, Harbin Institute of Technology at Weihai, Weihai 264209, China
[6]Department of Physics, Indian Institute of Technology Delhi, Hauz Khas, New Delhi 110016, India
[7]Tata Institute of Fundamental Research, 1 Homi Bhabha Road, Colaba, Mumbai 400 005, India

E-mail: *minchen@sjtu.edu.cn

Abstract. Structure and transportation of electron vortices in near-critical density plasmas driven by ultrashort intense laser pulses have been studied by multi-dimensional particle-in-cell simulations. Dimensional features of electron vortices are revealed. In two-dimensional geometry, two electron vortices and a quasi-static magnetic dipole are closely coupled. In three-dimensional geometry, a moving electron vortex ring associated with a closed magnetic ring moves in near-critical density plasmas. Such structure can transport some energy to the region where the laser pulse cannot reach. It is found that the motion of plasma ions makes the vortex magnetic energy dissipate quickly. These studies provide possible connection of electron vortices in nature with laser plasma experiments.
Keywords: PIC simulation, laser plasma interaction, electron vortex

1. Introduction

Linear and nonlinear structures generated during laser plasma interaction, such as laser wakefield [1, 2, 3], collisionless shockwaves [4, 5], postsolitons [6, 7] and magnetic vortices [8, 9], have drawn broad interests in experimental and theoretical studies. As one of the key parameters, plasma density largely determines the structure form. For underdense plasma, when ultrashort intense laser pulse propagates in it, a wakefield can be excited behind the pulse [1]. Such wakefield structure usually has high acceleration gradient and is widely used to accelerate electrons for the purpose of making compact accelerator and radiation source [3]. For near critical density (NCD) plasma, more kinds of nonlinear structures, like collisionless shockwaves, postsolitons, magnetic and electron vortices, can be generated when an intense laser pulse interacts with it. These coherent structures usually containing strong electromagnetic fields can survive for a long time and are normally considered disorganized and chaotic. However, they draw a lot of attention to research since they may induce significant energy transport and coupling. In some special region, these structures can be utilized to do laser ion acceleration and fundamental nonlinear physics studies. For example, particle-in-cell (PIC) simulations show that electron vortices can be generated at the boundary of a NCD plasma where the laser pulse propagates out of the plasma into the vacuum [10, 11] or the laser is obliquely incident on the plasma-vacuum boundary [12]. The vortices move perpendicular to the gradient of the plasma density and magnetic fields inside the vortices with intensity up to 10^4T are observed [11]. In recent years, with the development of foam target manufacture [13, 14] and application of supersonic gas jet [7, 15], NCD plasma can be generated in experiments, which creates realistic conditions to study these structures and may lead to wide applications. However, since the formation of such structures is a highly nonlinear process and they are sensitive to laser plasma parameters, it is quite difficult to predict their generation and dynamics, especially inside the plasma. Both theoretical and experimental studies are still needed for the clear understanding of these structures and their potential applications.

In this paper, by using multi-dimensional PIC simulations we study the generation and dynamics of electron vortex during the interaction of an ultrashort intense laser pulse with a NCD plasma. Unlike the previous studies focusing on the plasma-vacuum boundary region, we study the structures inside the plasma. Both two dimensional and three dimensional geometries are considered. We found that the generation mechanism of the vortex inside the plasma can be divided into two stages. Stage I: During the laser-plasma interaction, electrons are accelerated and form a strong axial electric current which is called as the drive current in the following. At the same time, strong charge separation fields and magnetic fields are also generated, which causes the curling of the drive current. Stage II: After the laser-plasma interaction, an electron void region is left and the ambient electrons move to this region to keep the electric neutrality. This process results in the formation of strong return currents. These currents are eventually coupled with the drive current and finally forms the vortex current forming electron vortices. Compared with the quasi-static vortex in 2D geometry, in 3D we found that the electron vortex can move forward along the laser propagation axis with a speed of $\sim 0.1c$, where c is the speed of light in vacuum. Such

structure gives a new form of laser energy transport to deep plasmas.

2. Generation of Electron Vortex in 2D Geometry

We use the relativistic PIC code OSIRIS [16] to perform multi-dimensional simulations. A circularly polarized laser pulse with wavelength of $\lambda_0 = 1.0\mu m$ and intensity of $I = I_0 exp(-r^2/R_L^2) exp[-(x - x_{cent})^2/c^2T^2]$ propagates along x direction. The amplitude of the laser intensity is $I_0 = 2.47 \times 10^{19} W/cm^2$, which corresponds to a normalized laser electric field of $a_0 = eE/m\omega c = 3.0$, where m, e, E, ω are electron mass and charge, laser electric field and frequency, respectively. The laser focus radius is $R_L = 3.6\mu m$ and the pulse duration is $T = 15.0fs$. The size of the simulation box is $32\mu m \times 16\mu m$ for 2D and $32\mu m \times 16\mu m \times 16\mu m$ for 3D simulations. It has been divided into 960×480 cells for 2D simulations and $640\times320\times320$ cells for 3D simulations. Such simulation boxes are large enough to ignore the nonphysical boundary effects during the whole simulation time. The initial laser pulse center and focus position are set at $x_{cent} = -10.0\mu m$ and $x = 5.0\mu m$, respectively. A plasma with upramp-plateau density profile is placed in the region of $0\mu m < x < 12.0\mu m$. The plasma density is uniformly distributed both along y and z directions. The initial density profile along the longitudinal direction can be seen from the inset of Fig. 1. The density around the upramp region linearly increases from 0 to $2.0n_c$ within $1.0\mu m$. The density in the plateau region is $2.0n_c$. Here $n_c = 1.1\times10^{21} cm^{-3}$ represents the critical density for the drive laser.

We firstly study the vortex generation with immobile ions. In stage I during the laser plasma interaction, electrons are accelerated

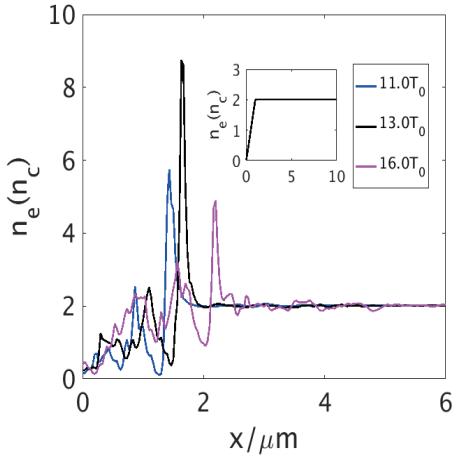

Figure 1. High-density electron layers formed during laser-NCD plasma interaction at $t = 11.0T_0$, $t = 13.0T_0$ and $t = 16.0T_0$. The inset shows the initial plasma density distribution along the x direction.

by the incident laser pulse. These electrons pile up in front of the laser pulse and form an electron layer with high density as shown in Fig. 1. The electron layer moves forward with a speed about $0.16c$. The electron layer density gets higher from $11.0T_0$ to $13.0T_0$, where T_0 represents the laser period. When the peak of the laser pulse arrives, more electrons are accelerated. After that, the electron layer gradually collapses and its density drops down. The laser drives such electrons to form longitudinal currents. As we will see later that such drive currents compose a part of the vortex current.

Since the laser initially has a Gaussian profile along the transverse direction, the electron layer is not uniform along the transverse direction as shown in Fig. 2(a). It shows that the electron layer density is higher on axis and gets smaller outwards. As we know, besides the longitudinal ponderomotive force, electrons also feel the radial ponderomotive force which has the form of $f_r \propto -\partial I/\partial r$. So the radial force gets maximum at $r = R_L/\sqrt{2} = 2.55\mu m$. When some electrons are

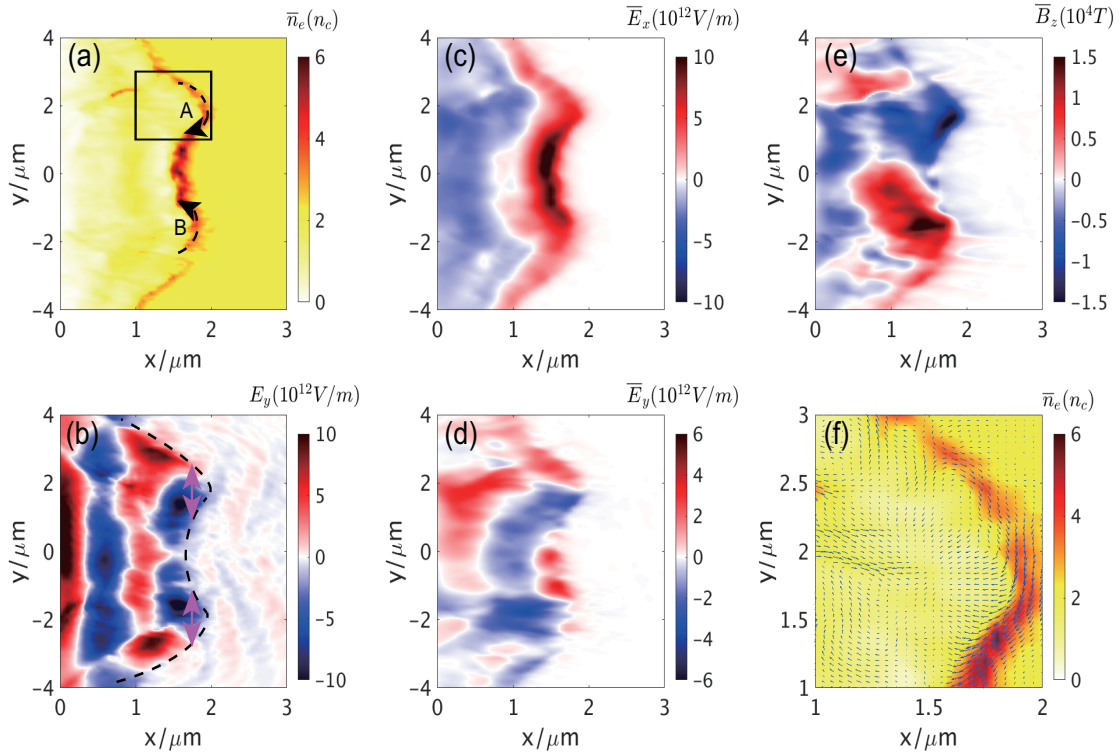

Figure 2. Spatial distributions of electron density $\overline{n}_e$ (a), laser electric field E_y (b), longitudinal electric field $\overline{E}_x$ (c), transverse electric field $\overline{E}_y$ (d), magnetic field $\overline{B}_z$ (e) and drive currents with the electron density background (f) at $t = 12.0T_0$. The region of the drive current distribution is labelled by the black rectangle in (a) and the dashed black arrows represent the drive currents. The overline "—" represents the mean value averaged within one laser period. The dashed black line in (b) represents the front of the laser pulse and the purple arrows represent the directions of the radial ponderomotive forces of the laser pulse whose front is bent due to the front electron layer.

repelled outward by this radial ponderomotive force, the remaining electrons are still accelerated forward by the longitudinal ponderomotive force, which bends the electron layer. The bent electron layer also reshapes the front of the laser pulse as shown in Fig. 2(b). Then it feeds back to f_r, which enforces the ponderomotive force and the curvature of the electron layer as marked by the dashed black line and purple arrows in Fig. 2(b). Finally a high density electron layer with a double raised structure is formed. The outward electrons move along this kind of curved layer forming a curled electron current as shown in Fig. 2(f).

On the other hand, the transverse and longitudinal charge separation fields ($\overline{E}_x$ and $\overline{E}_y$) form as shown respectively in Figs. 2(c) and 2(d). At the front region of the plasma target (i.e., the density upramp region), $\overline{E}_x$ can reach $\sim 10^{12}V/m$, while in the electron layer, it is close to $10^{13}V/m$. At the same time, a quasistatic magnetic field is generated in the laser plasma interaction region as shown in Fig. 2(e). The field is generated by the drive current along the electron layer. These quasistatic electric and magnetic (EM) fields can further bend the drive current through the $\vec{E} \times \vec{B}$ drift.

Besides the electrons moving in the layer, energetic electrons are also generated by direct

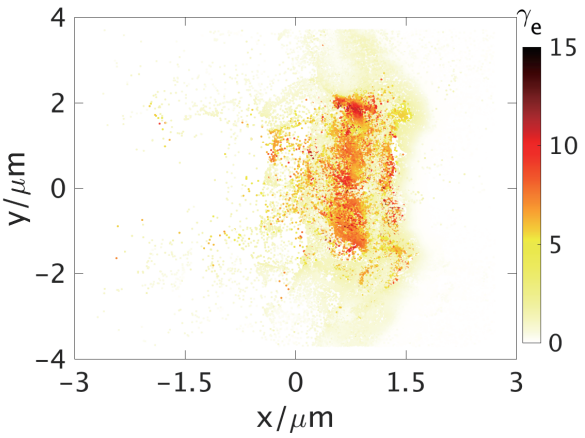

Figure 3. Spatial distribution of energetic electrons at $t = 12.0T_0$. The color represents the electron's energy in the unit of $m_e c^2$.

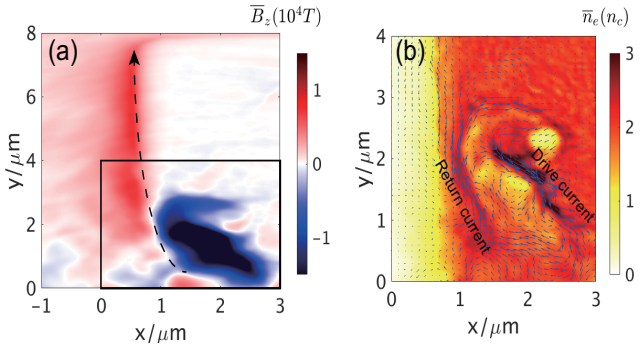

Figure 4. (a) Distribution of static magnetic fields inside the plasma at $t = 24.0T_0$. The return current is marked by the dashed black arrow. (b) The distribution of the return and drive currents vector within the region labelled by the black rectangle in (a). The background shows the distribution of the electron density.

acceleration of the incident and reflected laser pulses. A typical energy distribution of electrons in real space is given in Fig. 3. As one can see, the relativistic factor γ_e of the energetic electrons can be larger than 10. These high-energy electrons can not be confined within the laser-plasma interaction region. They leave the interaction region and build the charge separation force. With immobile ions in the simulation, the ambient electrons have to compensate this electron-void area and result in return currents. The return currents can last for tens of laser periods and the current vector is plotted in Fig. 4(b). When the return currents combine with the drive currents as shown in Fig. 4(b), an electron vortex forms inside the plasma. A magnetic field associated with these currents is found in the front part of the target as shown in Fig. 4(a). The intensity of the quasi-static magnetic field can reach $\sim 10^3 T$.

3. Structure of Electron Vortex and Fields in 2D Geometry

As described in above, the electron vortex can be generated by the combined drive and return currents around the penetration depth of the laser pulse. The structure evolves and a circle vortex shape finally forms. At $t = 120T_0$, the magnetic dipole structure and the associated electron vortices are formed as shown in Fig. 5. In our 2D simulation with immobile ions the magnetic dipole structure is almost stationary. Each magnetic pole is sustained by an associated electron vortex as shown in Fig. 5(d). Electrons trapped by the vortex undergo big cycle motions around the vortex center. Along with the big cycle motion, there are small cycles of Larmor motion as shown in Fig. 5(b). This kind of electron motion is due to the donut-like distribution of the radial charge separation field $\overline{E}_r$ and the magnetic field B_z of the vortex as shown in Fig. 5(c) and (d). With both $\overline{E}_r$ and B_z, the vortex electrons undergo $\vec{E} \times \vec{B}$ drift and the Larmor motion at the same time.

The generation of $\overline{E}_r$ is because electrons are expelled from the vortex center due to the magnetic pressure [10]. Figure 5(d) shows that the electron density in the vortex center is much lower than the density around the vortex edge. The static electric forces felt by the electrons are balanced by the centrifugal forces due to the big cycle motion.

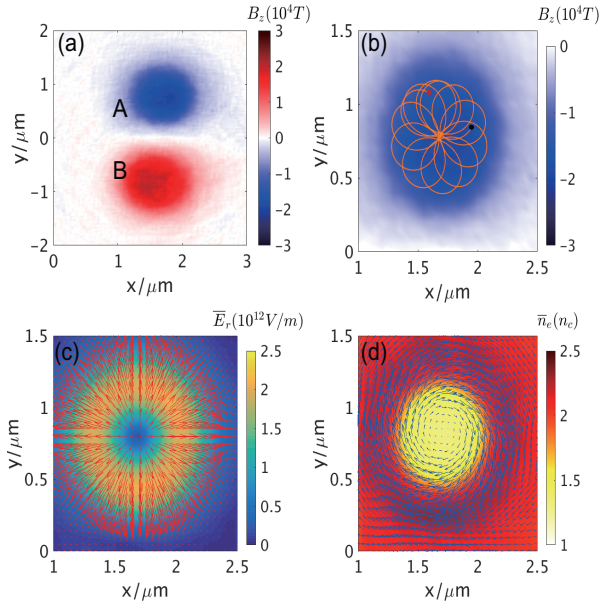

Figure 5. (a) Distribution of magnetic dipole structure with immobile ions background (magnetic field B_z component in Tesla) at $t = 120T_0$. (b) A typical trapped electron track in vortex A. Black point is the initial position and red point represents the final position. (c) Radial electric vector (red arrows) and field E_r of vortex A. (d) Electron density distribution and electric current vector (blue arrows) of vortex A.

The electron dynamics inside the vortex can be well described by the electron magneto-hydrodynamic (EMHD) model [17]. The basic EMHD equation can be written as

$$\frac{\partial}{\partial t}(\vec{B} - \nabla^2\vec{B}) = \nabla \times [\vec{v}_e \times (\vec{B} - \nabla^2\vec{B})] \qquad (1)$$

where $\vec{v}_e$ is electron fluid velocity. A typical stationary solution by neglecting the displacement current (i.e. $\nabla \times \vec{B} = -\mu_0 n_e e \vec{v}_e$) in 2D geometry (i.e. $\vec{B} = \overline{B}_z \vec{e}_z$, where $\vec{e}_z$ is the unit vector along z direction) is [18]

$$\overline{B}_z = B_0 \exp(-r^2/R^2) \qquad (2)$$

where the cylindrical coordinates (r, θ, z) are used to describe the vortex structure and R represents the characteristic scale length of $\overline{B}_z$. From the balance condition of electrons one can get the radial electric field $\overline{E}_r$ as [18]

$$\overline{E}_r = E_0 r \exp(-2r^2/R^2), \qquad (3)$$

which shows a donut-like distribution.

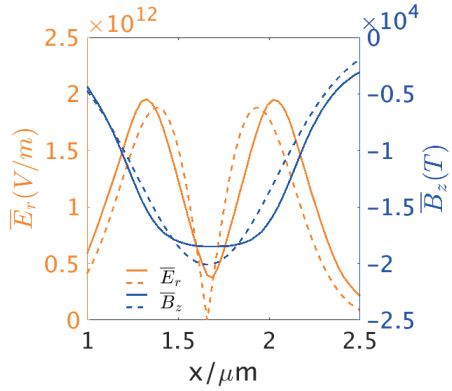

Figure 6. Distributions of the radial electric field $\overline{E}_r$ and the magnetic field $\overline{B}_z$ at $y_c = 0.75\mu m$ which is cut right through the vortex center. The solid lines represent the simulation results and the dashed lines represent the fitted curves.

In Fig. 6 we show the fields distribution of the vortex from the simulation results. We fit the distribution lines according to Eq.(2) and Eq.(3) to get the vortex size R. As one can see that the theoretical curves fit both fields quite well and they give $B_0 = -2 \times 10^4 T$, $E_0 = 1.13 \times 10^{13} V/m$, $R = 0.55\mu m$. The Larmor radius $r_L < m_e c/\overline{B}_z(R)e = 0.23\mu m$ at $r = R$ which is smaller than R. The electrons can be well trapped inside the vortex by the fields and make the structure last for a long period until the ions' motion cannot be neglected any more.

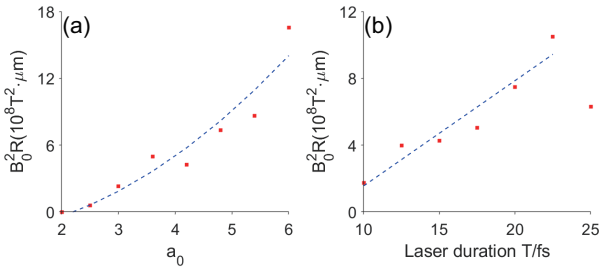

Figure 7. Variation of the magnetic energy ($\propto B_0^2R$) inside the vortex along with the laser intensity (a_0) for pulse duration of $T = 15.0$fs (a) and with the pulse duration (T) for $a_0 = 4.2$ (b).

To see the universality of such kind of vortex structure in laser plasmas, simulations with different laser intensities and pulse durations have been performed. The results are shown in Fig. 7. With the laser intensity (a_0) and duration (T) increasing, more laser energies can be transmitted to the vortex. In 2D geometry, the magnetic energy ϵ_B of the electron vortex with characteristic size R satisfies $\epsilon_B \propto 2\pi B_0^2 \int_0^{+\infty} \exp(-2r^2/R^2)dr \propto \pi^{3/2}B_0^2R/\sqrt{2}$. As one can see from Fig. 7, ϵ_B is proportional to the pulse energy, i.e. a_0^2 and T. However, when a_0 increases further, the electron layer forming the drive current can be damaged and a stable vortex cannot be formed. On the contrary, when the laser intensity is too small, there is no vortex structure. For the laser pulse duration, when it increases further, the return current around the laser plasma interaction region will be weaken due to the current suppression resulting from the laser ponderomotive force. In this case, the vortex magnetic energy ϵ_B gets smaller as indicated by the last point (T=25fs) in Fig. 7(b).

4. Structure and Dynamics of Electron Vortex and Fields in 3D Geometry

We also investigated the electron vortex generation and dynamics in 3D geometry. Both the drive currents and return currents including the associated magnetic field have been observed in 3D simulations. Unlike the magnetic dipole structure in 2D geometry, a $smoke-ring-like$ magnetic structure is formed in 3D case as shown in Fig. 8(a). It is natural to see that in the $x-y$ projection plane there is a magnetic dipole structure. The magnetic fields and electron vortices are shown in Figs. 8(b) and 7(c), respectively. These structures are very similar as those in 2D simulations. However, unlike the central stationary electron vortex in 2D geometry, the ring structure in 3D moves forward along the x axis with a speed close to $V_X \sim 0.1c$ as labeled by the black arrows in Figs. 8(a) and 7(b). As one can see in Fig. 8(b), there are magnetic remnants behind the electron vortex when it moves forward. Such forward moving speed cannot be simply explained by the usual Hall speed deduced from the EMHD model, since the Hall speed is proportional to the gradient of electron density [17, 19] which is zero here. From the simulation, we found that actually the initial speed of the electron vortex is driven by the axial current generated during the laser-electron acceleration. However, the laser pulse can only accelerate the electrons inside the plasma before it is totally reflected. Once the electron vortex moves forward, some electrons in front of the vortex will be trapped in it and this gradually depletes the vortex's magnetic energy. As one can see from Fig. 8(d), the magnetic energy of the vortex dissipates linearly along with the time, which induces the electric field through the Faraday effect: $\nabla \times \vec{E}_X = -\partial \vec{B}_\varphi/\partial t$. These electric

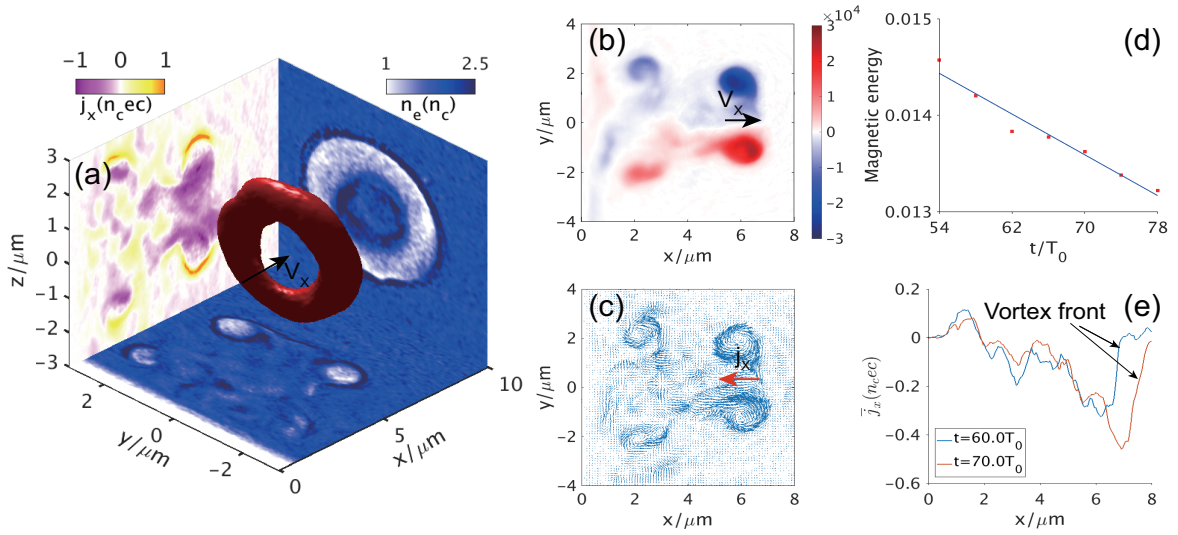

Figure 8. (a) The *smoke-ring-like* structure of 3D electron vortex with immobile ions background at $t = 60.0T_0$. The red isosurface shows the toroidal magnetic field with strength of $|\vec{B}_\varphi| = 1.7 \times 10^4 T$. Both $x-y$ and $y-z$ slices are cut through the center of the vortex. The longitudinal electric current density of the vortex is shown in $x-z$ plane. (b) Distribution of magnetic field in Tesla and (c) its associated electron vortex in $x-y$ plane. (d) Dissipation of magnetic energy (normalized to the laser energy) of electron vortex with simulation time. (e) Distribution of axial current $\bar{j}_x$ (averaged within $1.0T_0$) on axis at $t = 60.0T_0$ and $t = 70.0T_0$.

fields then accelerate electrons along the axis. Finally an axial current j_X is accompanied with the vortex as labeled by the red arrow in Fig. 8(c). It drives the vortex to continuously move forward. The moving speed depends on the spatial distribution and energy dissipation of the magnetic fields in the ring. The longitudinal currents at two different instants are shown in Fig. 8(e). Such current in 2D geometry is not strong enough to drive the magnetic dipole structure to move forward due to the dimensional effects. As a result, in 2D simulations, no obvious magnetic dissipation and vortex motion can be observed.

5. Ion motion effects on vortex dynamics

In the above studies, the background ions are immobile. This assumption is only reasonable when we discuss the vortex generation and motion in a relatively short period compared with the ion motion time. For a long period description of vortex dynamics, we studied a fully ionized carbon plasma case with completely ionized carbons, i.e. C^{6+}, in 3D geometry. The simulation results are shown in Fig. 9. As labeled in Fig. 9(a) and (b), a forward moving ring-like magnetic structure and the associated electron vortex are observed in the simulations. However, the intensity of the magnetic field is much weaker compared to the field observed in the case with immobile ions. On the contrary, the magnetic remnants behind the moving vortex is much stronger. Finally, a big vortex structure is found behind the small one. It seems like that the small moving vortex elongates the remnants. Since the ions' motion is taken into account in this simulation, the electric and magnetic fields of the electron vortex shown in Figs. 5(c) and 5(d) can accelerate both of the ions and electrons. As one can see from Fig. 9(c), a

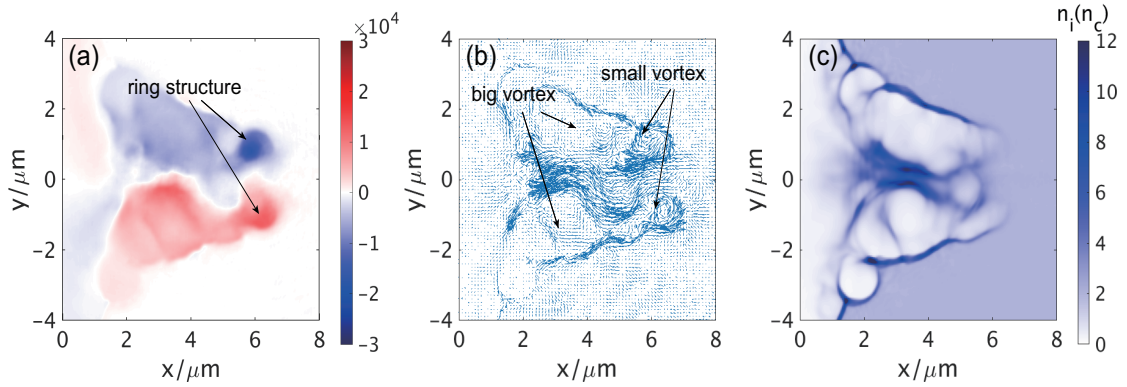

Figure 9. Spatial distributions of the magnetic field (a) and its associated electron vortex (b) with mobile ions C^{6+} in $x-y$ plane. (c) Spatial distribution of the ion density n_i at $t = 60.0T_0$.

plasma channel with central ion filament forms when the electron vortex propagates inside the plasma. Although the ions cannot get much energy from the fields compared to the electrons due to the heavier mass, it does cause the faster dissipation of the magnetic energy than the case with immobile ions. The dynamic process becomes more complicated in this situation. To better understand the dynamics, more further works are needed.

6. Conclusion and Discussion

In conclusion, the generation and dynamics of electron vortices inside the plasma during an ultrashort intense laser interacting with a NCD plasma target have been numerically studied. With immobile ions, in 2D geometry, the incident laser directly accelerate electrons and an electron layer is formed and moves forward forming the drive current. The charge separation field induces the return currents. The two currents excite the electron vortex and the associated magnetic dipole structure inside the plasma. In 3D geometry, the vortex shows a $smoke-ring-like$ structure and moves forward inside the plasma, which is driven by an axial electric current. With mobile ions, a forward-moving vortex inside the plasma still exists but the magnetic energy dissipates faster than the case with immobile ions. At the same time, a big electron vortex with stationary center is found behind the forward-moving vortex. The vortex motion makes it a potential carrier to transport magnetic energy to deep plasmas where the laser pulse cannot reach. Although such kind of magnetic energy transportation has been observed before in 2D geometry, however, it depends on the density gradient of the plasma [20]. While our results show that the such energy transportation is self-sustained in 3D geometry even in homogeneous plasmas.

In further, as it is known, besides in laser plasmas, vortex structures are also very common in nature and interstellar space. For example, Kelvin-Helmholtz instability always introduces rolled-up vortices in Earth's magnetosphere. Such vortex is significant for plasma transportation on the magnetopause [21]. With the development of laser plasma physics, in recent years laboratory astrophysics have been developed very quickly, such as studies on magnetic reconnection [22], outflows in solar flares [23] and Weibel instability [24, 25, 26, 27]. However, the lab-

oratory study of astrophysics related vortex structure in laser plasma interaction, especially with femto-second laser system, is still lacking. The current study may help to generate similar structures in laboratory and provide a potential way for fundamental laboratory astrophysics studies.

7. Data availability statements

The data that support the findings of this study are available upon reasonable request from the authors.

Acknowledgments

This work was supported in part by NSFC (11991074, 11774227), NSAF (U1930111) of China, the Science Challenge Project (No.TZ2018005), the Strategic Priority Research Program of Chinese Academy of Sciences (XDA25000000), and Natural Science Foundation of Shandong Province (ZR2019ZD44). MC acknowledges the support from Shanghai Municipal Government (No. 18JC1410700). AD and GRK acknowledge partial support from SERB, Govt. of India through their respective J C Bose Fellowship grants JCB/2017/ 000055/2017 and JCB-037/2010. AD also acknowledges partial support from CRG/2018/000624. Simulations were performed on the Π supercomputer at Shanghai Jiao Tong University. The authors would like to acknowledge the OSIRIS Consortium, consisting of UCLA and IST (Lisbon, Portugal) for the use of OSIRIS and the visXD framework.

References

[1] Tajima T and Dawson J M 1979 *Phys. Rev. Lett.* **43** 267
[2] Esarey E, Schroeder C B and Leemans W P 2009 *Rev. Mod. Phys.* **81**, 1229
[3] Chen M, Liu F, Li B Y, Weng S M, Chen L M, Sheng Z M and Zhang J 2020 *High Power Laser and Particle Beams* **32**, 092001
[4] Denavit J 1992 *Phys. Rev. Lett.* **69** 3052
[5] Haberberger D, Tochitsky S, Fiuza F, Gong Ch, Fonseca R A, Silva L O, Mori W B and Joshi C 2012 *Nat. Phys.* **8** 95
[6] Esirkepov T, Nishihara K, Bulanov S V and Pegoraro F 2002 *Phys. Rev. Lett.* **89** 275002
[7] Sarri G *et al* 2010 *Phys. Rev. Lett.* **105** 175007
[8] Nakamura T, Bulanov S V, Esirkepov T Zh, and Kando M 2010 *Phys. Rev. Lett.* **105**, 135002
[9] Helle M H, Gordon D F, Kaganovich D, Chen Y, Palastro J P and Ting A 2016 *Phys. Rev. Lett.* **117** 165001
[10] Bulanov S V and Esirkepov T Zh 2007 *Phys. Rev. Lett.* **98** 049503
[11] Bulanov S V, Dylov D V, Esirkepov T Zh, Kamenets F F and Sokolov D V 2005 *Plasma Phys. Rep.* **31** 369
[12] Yi L Q, Pusztai I, Pukhov A, Shen B F, and Fülöp T 2019 *J. Plasma Phys.* **85**, 905850403.
[13] Fournier K B, Constantin C, Poco J, Miller M C, Back C A, Suter L J, Satcher J, Davis J and Grun J 2004 *Phys. Rev. E* **92** 165005
[14] Li Y T *et al* 2005 *Phys. Rev. E* **72** 066404
[15] Romagnani L *et al* 2010 *Phys. Rev. Lett.* **105** 175002
[16] Fonseca R A *et al.* 2002 *Lect. Notes Comput. Sci.* **2331**, 342
[17] Yadav S K, Das A and Kaw P 2008 *Phys. Plasmas* **15** 062308
[18] Hata M, Sakagami H and Das A 2013 *Phys. Plasmas* **20** 042303
[19] Rudakov L I and Huba J D 2002 *Phys. Rev. Lett.* **89** 095002
[20] Yadav S K, Bera R K, Verma D, Kaw P and Das A 2020 *Contrib. Plasma Phys.* e202000101
[21] Hasegawa H, Fujimoto M, Phan T -D, Rème H, Balogh A, Dunlop M W, Hashimoto C and TanDokoro R 2004 *Nature* **430** 755
[22] Li C K, Séguin F H, Frenje J A, Rygg J R, Petrasso R D, Town R P J, Landen O L, Knauer J P and Smalyuk V A 2007 *Phys. Rev. Lett.* **99** 055001
[23] Zhong J *et al* 2010 *Nature Physics* **6** 984
[24] Huntington C M *et al* 2015 *Nature Physics* **11** 173
[25] Fox W, Bhattacharjee A, Chang P -Y, Germaschewski K, Hu S X and Nilson P M 2013 *Phys. Rev. Lett.* **111** 225002

[26] Mondal S *et al* 2012 *Proc Natl Acad Sci USA* **109** 8011

[27] Chatterjee G, Schoeffler K M, Singh P K, Adak A, Lad A D, Sengupta S, Kaw P, Silva L O, Das A and Kumar G R 2017 *Nature Communications* **8** 15970